MRS Communications (2018), *8*, 1178–1183
© Materials Research Society, 2018
doi:10.1557/mrc.2018.180

MRS Communications

Research Letter

Study and modeling of melt pool evolution in selective laser melting process of SS316L

J. L. Tan, Singapore Centre for 3D Printing, School of Mechanical and Aerospace Engineering, Nanyang Technological University, 50 Nanyang Avenue, Singapore 639798, Singapore; SLM Solutions Singapore Pte. Ltd., 25 International Business Park, #02-15/17 German Centre, Singapore 609916, Singapore **C. Tang,** and **C. H. Wong,** Singapore Centre for 3D Printing, School of Mechanical and Aerospace Engineering, Nanyang Technological University, 50 Nanyang Avenue, Singapore 639798, Singapore

Address all correspondence to C. H. Wong at **CHWong@ntu.edu.sg**

(Received 27 May 2018; accepted 15 August 2018)

Abstract

In this paper, the melting of stainless steel 316L using Computational Fluid Dynamics to observe the melt pool characteristics is studied. The simulation model allows the observation of the molten pool flow during the selective laser melting process due to Marangoni's effect and recoil pressure. Furthermore, different parameters are tested to show their effects on the melt pool and track formation. Different laser powers, as well as scanning speeds, were used to study the effects they have on the melt pool characteristics. The results were used to determine the relationships between these factors and the melt pool characteristics.

Introduction

Selective laser melting (SLM) manufactures a three-dimensional (3D) object by adding layer upon layers.[1] In SLM, a layer of powder is deposited and the laser will scan at the areas marked in the sliced stereolithography file. Once the laser has completed the scanning, a fresh layer of powder will be deposited and the process will repeat until the part is completed. It has seen applications in various industries such as aerospace, automotive as well as medical.[2,3] Its freedom of design allows the incorporation of lattice structures to produce lightweight parts.[4,5]

SLM is a complex process which involves numerous parameters such as laser power, scanning speed, hatch spacing, layer, and scanning strategy. These parameters contribute to the energy density applied on the powder bed, and will affect the quality of the part.[6–8] Gan and Wong observed that by varying the layer thickness, the porosities and the mechanical properties of the printed parts are affected.[9] However, it was found that parameters such as the scanning speed and laser power exhibit larger influence over the part's properties.[10]

Relying on experiments to conduct parametric studies can be costly and time-consuming. The use of numerical modeling can assist in determining the optimum sets of processing parameters. Khairallah et al. made use of a numerical model to study the Plateau–Rayleigh instability phenomena on the continuity of the melt track.[11] Kruth et al. explained the melt pool will tend to reduce its free surface energy. The melt pool can be treated as a half cylinder and when the total surface of the melt pool exceeds that of a sphere with the same volume, it will break to form spheres known as the balling phenomena.[12]

Mechanical properties of the printed part can be affected by the melt pool. When a deep keyhole is formed by high energy density, the keyhole will become unstable and collapse, while trapping gas within the melt pool.[13] This will give rise to porous parts. Kempen et al. observed that fractures are initiated by pores near the surface of the printed part.[14] AlMangour et. al. noted that the melt pool affects the hardness and the grain sizes of the printed part.[15] Another importance of the melt pool is its effect on microstructure evolution. The melt pool can affect the local thermal gradient, which in turn influences the growth rate of the microstructures.[16]

In view of the above, this paper looks at how different processing parameters will affect the melt pool and track formation. These investigations will reveal the relationships between the different characteristics of the melt pool, which in turn will affect the mechanical properties of the printed part.

Methodology

To numerically generate the powder bed, a Discrete Element Method model using LIGGGHTS® software was carried out.[17] The powder size follows a Gaussian distribution of mean diameter 27 μm with a full width at half maximum value of 5 μm. The powders were released from a height of 700 μm onto a 1000 × 200 × 200 μm substrate to simulate the random scattering of powders observed in the actual experiment. The coordinates and the radii of individual powders are extracted and input into a CFD software (OpenFOAM®) which is capable of modeling the melting and solidification process.

OpenFOAM® (Open Field Operation and Manipulation) is an open-source Computational Fluid Dynamics toolbox

https://doi.org/10.1557/mrc.2018.180 Published online by Cambridge University Press

Table 1. Parameters used

Run	Laser power (W)	Scanning speed (m/s)
1	100	1
2	100	3
3	300	1
4	300	3

which is used in the present study to model the SLM process.[18] The metal used in the simulation is SS316L. The mesh size used in the simulations was 2.5 μm. The parameters used for the single-track model for different runs are shown in Table 1. Table 2 shows the physical properties of SS316L and the constants used for the modeling. In the model, a timestep of 10 ns were used. The length of each track was 800 μm. The data from each simulation were extracted and plotted against each other for comparisons.

Thermal fluids equations

There are two different phases in the model, metallic and gas phase. The volume of fluid method was used to distinguish between the metallic and gas phases.[19] The phase fraction, α, is used to distinguish the different phases present in the simulation. The relationship is given as

$$\alpha_1 + \alpha_2 = 1 \tag{1}$$

where the metallic phase is represented by α_1 and the gas phase is represented by α_2.

In the metallic phase, the metal can exist in the solid or liquid state. To determine the state of the metal, a liquid fraction, γ was introduced.[20] The values of γ lies between 0 and 1. When $\gamma = 0$, the metal is in the solid state. When $\gamma = 1$ the metal is in the liquid state. Any values between 0 and 1 will be referred as the mushy state.

In the simulation, there will be meshes which comprise air and metal mixture. In this region, the average material property, $\bar{\varphi}$, is used and is calculated using

$$\bar{\varphi} = \varphi_{\text{air}} \cdot \alpha_2 + \varphi_{\text{metal}} \cdot \alpha_1 \tag{2}$$

where φ_{air} is the material property for air and φ_{metal} is the material of the metal. An example of the volume average of the density is given by $\bar{\rho} = \rho_{\text{air}} \cdot \alpha_2 + \rho_{\text{metal}} \cdot \alpha_1$.

There are three main governing equations used in the model. They are the conservation of mass, conservation of momentum, and conservation of energy equations. The metal was assumed to be incompressible and therefore the continuity equation can be represented by

$$\nabla \cdot \vec{\boldsymbol{u}} = 0 \tag{3}$$

where $\vec{\boldsymbol{u}}$ is flow velocity.

Table 2. Physical properties of SS316L and constants used in the simulations.

Physical properties	Values
Solidus temperature (K)	1658
Liquidus temperature (K)	1723
Boiling temperature (K)	3090
Surface tension (N/m)	1.6
Coefficient of surface tension (N/m/K)	8×10^{-4}
Base thermal conductivity of solid (W/m/K)	9.248
Base thermal conductivity of liquid (W/m/K)	12.41
Reference temperature (K)	300
Base density of liquid (kg/m^3)	7433
Base density of solid (kg/m^3)	8084
Specific heat of solid metal (J/kg/K)	462
Specific heat of liquid metal (J/kg/K)	775
Latent heat of fusion (J/kg)	2.7×10^6
Latent heat of vaporization (J/kg)	7.45×10^6
Emissivity	0.26
Convective coefficient (W m^2 K)	80
Darcy term coefficient (kg/m^3/s)	1×10^6
Stefan-Boltzmann's constant (W/m^2/K^4)	5.67×10^{-8}
Universal gas constant (J/K/mol)	8.3144
Atmospheric pressure (N/m^2)	101,000
Molar mass (kg/mol)	0.05593

For the conservation of momentum, the forces acting on the system are considered. The recoil pressure, Marangoni force, buoyancy force, surface tension, and gravitational force can be found on the right-hand side of[21]

$$\begin{aligned}\frac{\partial \bar{\rho}\vec{\boldsymbol{u}}}{\partial t} + \nabla \cdot (\bar{\rho}\vec{\boldsymbol{u}} \otimes \vec{\boldsymbol{u}}) = &-\nabla p \\ &+ \nabla \cdot (\bar{\mu} \cdot \nabla \vec{\boldsymbol{u}}) + \bar{\rho} g \hat{e}_z \beta (T - T_{\text{ref}}) - K_c \left[\frac{(1-\gamma)^2}{\gamma^3 + C_k}\right]\vec{\boldsymbol{u}} \\ &+ \left\{\sigma k \hat{n} + \frac{d\sigma}{dt}[\nabla T - \hat{n}(\hat{n} \cdot \nabla T)] + p_v\right\}|\nabla \alpha_1| \frac{2\bar{\rho}}{(\rho_{\text{metal}} + \rho_{\text{air}})}\end{aligned} \tag{4}$$

where $\bar{\rho}$ is the volume average of density, $\bar{\mu}$ is the volume average of viscosity, t is the time, T is the temperature, T_{ref} is the reference temperature, p is pressure, g is gravitational acceleration, and p_v is the recoil pressure. $\hat{e}_z$ is the unit normal to the gravitational force, β is the thermal expansion coefficient, and

https://doi.org/10.1557/mrc.2018.180 Published online by Cambridge University Press

K_c is the permeability coefficient. C_k is a constant to avoid division by zero, σ is the surface tension, and k is the surface curve normal to $\hat{n}$. $|\nabla\alpha_1|$ was used to transform a surface force per unit area into a volumetric surface force.[22,23]

The Marangoni force is expressed as $(d\sigma/dt)[\nabla T - \hat{n}(\hat{n}\cdot\nabla T)]$. From the equation, it shows that the force is temperature dependent. In the melt pool, the temperature gradient will result in a difference in surface tension.[24] The molten metal will flow from the region with low surface tension to a region with high surface tension.

During the laser melting process, the surface of the molten metal may reach over the boiling point of the metal. The metal will vaporize and exerts a downward pressure on the melt pool, commonly observed as the keyhole phenomena. This pressure is known as the recoil pressure and is defined by[25]

$$p_v = 0.54 p_0 \exp\left(\Delta H_V \cdot M \frac{T - T_{LV}}{RTT_{LV}}\right) \tag{5}$$

where p_0 is the atmospheric pressure, ΔH_V is the enthalpy change due to vaporization, M is the molar mass of the metal, T_{LV} is the evaporation temperature of the metal, and R is the universal gas constant.

In the model, the heat transfer due to conduction, convection, radiation, laser input, and phase transformation are represented in the conservation of energy equation, given by

$$\begin{aligned}\frac{\partial \bar{C}_p\bar{\rho}T}{\partial t} + \nabla\cdot(\vec{u}\bar{C}_p\bar{\rho}T) = &-\frac{\partial\bar{\rho}\Delta H_f}{\partial t} - \nabla\cdot(\bar{\rho}\vec{u}\Delta H_f)\\ &+ \nabla\cdot(\bar{k}\nabla T) + Q_T - [h_c(T - T_{\text{ref}}) + \sigma_s\varepsilon(T^4 - T_{\text{ref}}^4)\\ &+ Q_v]|\nabla\alpha_1|\frac{2\bar{C}_p\cdot\bar{\rho}}{(C_{p(\text{metal})}\cdot\rho_{\text{metal}} + C_{p(\text{air})}\cdot\rho_{\text{air}})}\end{aligned} \tag{6}$$

where Q_T is the laser input, ΔH_f is the enthalpy change due to fusion, $\bar{k}$ is the volume average of thermal conductivity, h_c is the heat transfer coefficient, $\bar{C}_p$ is the volume average of specific heat, σ_s is the Stefan–Boltzmann constant, ε is the emissivity, Q_v is the heat loss due to evaporation. The term $-(\partial\bar{\rho}\Delta H_f/\partial t) - \nabla\cdot(\bar{\rho}\vec{u}\Delta H_f)$ is the enthalpy change due to the melting of the metallic phase. The conduction, convection, and radiation are given by $\nabla\cdot(\bar{k}\nabla T)$, $h_c(T - T_{\text{ref}})$, and $\sigma_s\varepsilon(T^4 - T_{\text{ref}}^4)$, respectively.

The laser beam intensity can be approximated as a Gaussian distribution given by

$$I = \frac{2\eta P}{\pi r^2}\exp\left[-2\frac{(x + v\cdot t - x_0)^2 + (y - y_0)^2}{r^2}\right] \tag{7}$$

where η is the absorptivity coefficient, p is the laser power, x and y are the coordinates of the center of the laser beam at time t, x_0, and y_0 are the starting coordinates of the laser beam, r is the radius of the laser beam, and v is the scanning speed. The radius of the laser beam for the simulation is set to be 27 μm and the absorptivity was taken to be 0.4.

To obtain the laser beam energy density, the intensity of the beam can be approximated as

$$Q_T = \frac{I\cdot f_{\text{absorb}}}{\Delta z} \tag{8}$$

where Δz represents the height of the numerical grid and f_{absorb} is an indicator ranging from 0 to 1 to ensure the heat flux is only applied on the top surface of the metal. Further explanation of f_{absorb} can be found in the supplementary material. In this model, the Fresnel absorption was neglected due to the high computational cost.

In the laser process, the prominence of evaporation increases along with temperature increase and cannot be neglected. Therefore, the heat loss due to evaporation is defined

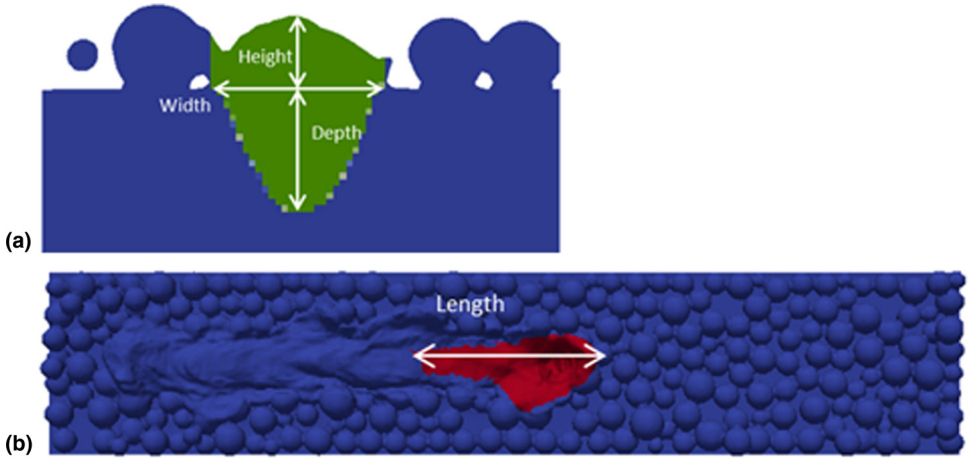


Figure 1. Measurements of the melt pool's dimension on the 1000 × 200 × 200 μm substrate model. (a) Green represents the solidified track and (b) red region represents the molten metal.

https://doi.org/10.1557/mrc.2018.180 Published online by Cambridge University Press

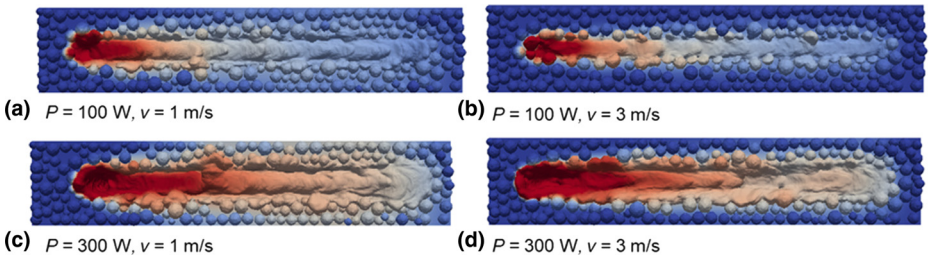


Figure 2. Top view of the tracks of (a) run 1, (b) run 2, (c) run 3, and (d) run 4.

Table 3. Dimensions of melt pools

Run	Height (μm)	Width (μm)	Depth (μm)	Length (μm)	Length/width
1	15	72.5	35	135	1.8
2	10	57.5	7.5	116	2
3	12.5	77.5	130	265	3.4
4	7.5	87.5	47.5	252.5	2.8

as[25]

$$Q_v = 0.82\frac{\Delta H_v \cdot M}{(2\pi MRT)^{0.5}} p_0 \exp\left(\Delta H_v \cdot M \frac{T - T_{LV}}{RTT_{LV}}\right) \quad (9)$$

Results and discussions

Figure 1 illustrates how the measurements of the dimensions were taken for Table 2. Figure 1(a) shows the cross-section of a solidified track (green region) when measuring the height, width, and depth of the melt pool. Fig. 1(b) shows the red region representing the molten metal to record the reading of the length of the melt pool. Figure 2 shows the top view of the melt tracks. The dimensions of the melt pool are shown in Table 3. Comparing Figs. 2(a) and 2(c) to Figs 2(b) and 2(d) respectively, it can be observed that increasing the scanning speed from 1 m/s to 3 m/s will induce narrower tracks. Since the melt pool generated from a higher scanning speed is smaller than that of a lower scanning speed, it will affect the width of the melt track. With a narrower track width, the hatch spacing will have to be reduced to avoid unmelted regions between tracks. From the energy density equation,[26] it can be noted that despite run 1 and run 4 sharing the same energy density, their melt track profiles vary significantly with run 4 having a wider melt pool. Therefore, it shows that the parameters have different impacts on the melt pool. This is in agreement with the experimental observation by Bertoli et al.[27] In their experiments, the track with a lower laser power and scanning speed displayed a more consistent melt profile. Similarly from this model, Fig. 2(a) has a smoother melt surface when compared with Fig. 2(d). In Fig. 3, the heights of the tracks were measured and plotted to show the mean and deviations which relate to the surface roughness of the track. A greater deviation would directly translate to a rougher surface of the track. The difference in surface roughness can be explained using Rayleigh–Plateau instability principle. It occurs due to the effect of surface tension. The melt pool can be observed as a semi-cylindrical fluid. When the length to width ratio of the melt pool increases beyond a critical value of 2.1, it will result in Raleigh–Plateau instability.[12,28] If the melt pool is long, it will result in necking and breaking of the semi-cylindrical shape, resulting in unevenness of the melt pool profile. In Table 3, the lengths of the melt pool

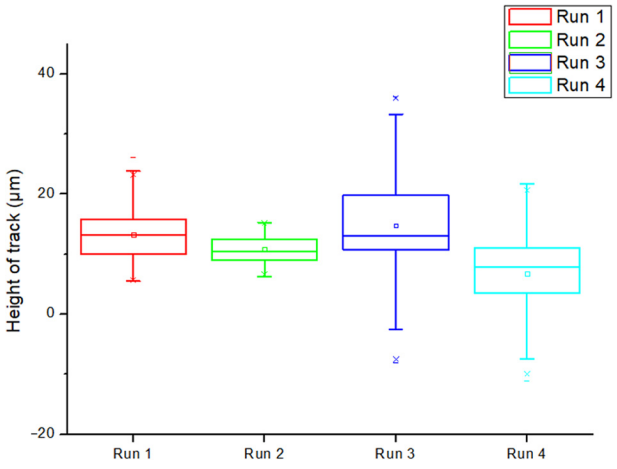


Figure 3. Heights of tracks along the scanning direction.

https://doi.org/10.1557/mrc.2018.180 Published online by Cambridge University Press

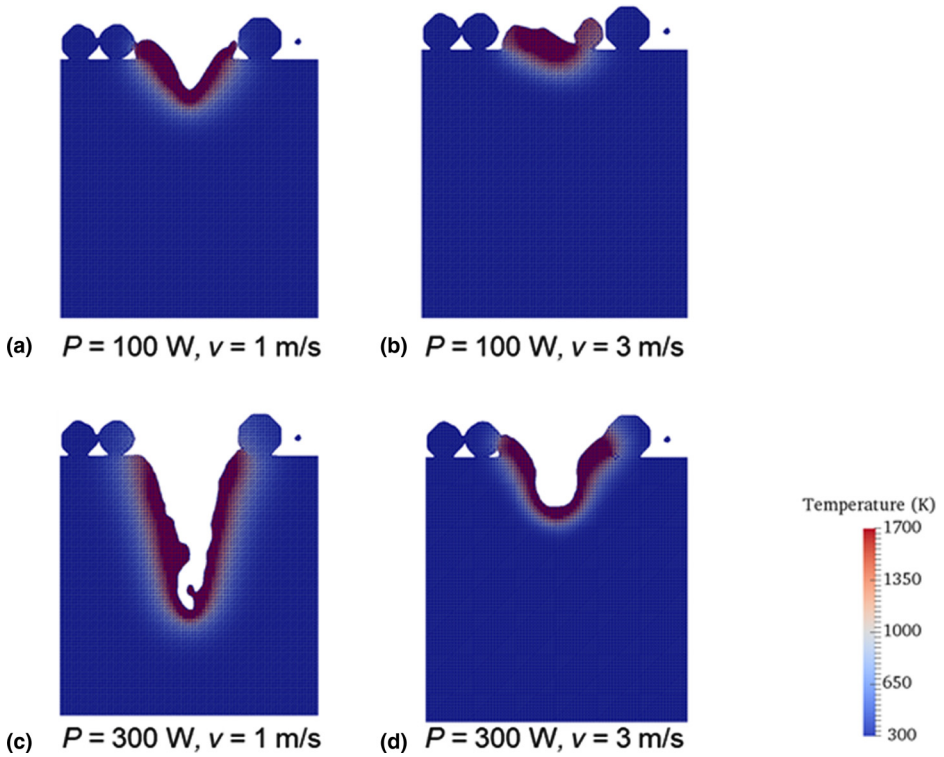


Figure 4. Cross-sections of melt pool of (a) run 1, (b) run 2, (c) run 3, and (d) run 4.

were measured. Comparing the length of the melt pools to the surface roughness, a positive correlation can be established.

Figure 4 shows the cross-section of the melt pool during the melting process. Comparing Figs. 4(a) and 4(c), it was observed that the laser power primarily affects the depth of the melt pool. The widths of run 1 and 3 are approximately similar, while their depths differ significantly. Taking Run 2 as an example, increasing the laser power to 300 W will achieve a greater impact on the resultant depth than reducing the scanning speed to 1 m/s. In run 1, the low scanning speed will result in heat being conducted away from the melt pool. Temperature around the melt pool will be lowered leading to a reduction in the vaporization of the molten metal. This will lead to a decrease in recoil pressure and giving a shallower depth. In run 4, the high laser power will be absorbed by the metal, resulting in its temperature soaring above the boiling point. The higher rate of metal vaporizing will increase the recoil pressure and therefore, leading to a deeper depth. When comparing the effects of laser power and scanning speed on the width of the track, varying the laser power from 100 W to 300 W will give a wider melt pool than using a lower scanning speed of 1 m/s. A similar conclusion can be drawn from experimental results.[29]

Conclusions

In this paper, the use of simulation is able to show the relationship between the length of the melt pool with the resultant surface roughness of the track. A longer melt pool will give rise to a rougher surface due to the instability of the melt pool.

Next, it can be concluded that laser power has more effect over the width and depth of the melt pool. Similar conclusions can be derived from experimental studies by Yadroitsev et al.[29] This shows that modeling of SLM process can aid in the parametric study of SLM and provide a good representation of the experiments. It can help to reduce the time and materials cost of conducting experiments.

Supplementary Material

The supplementary material for this article can be found at https://doi.org/10.1557/mrc.2018.180

Acknowledgements

The work is funded by SLM Solutions Group AG (RCA-14/089) in collaboration with Singapore Centre for 3D Printing, Nanyang Technological University, Singapore. The work is also supported by EDB-IPP and SLM Solutions Singapore Pte Ltd.

Conflict of interest

The authors declare no conflict of interest.

References

1. M. X. Gan and C. H. Wong: Practical support structures for selective laser melting. *J. Mater. Process. Technol.* **238**, 474–484 (2016).

https://doi.org/10.1557/mrc.2018.180 Published online by Cambridge University Press

2. C. K. Chua, C. H. Wong, and W. Y. Yeong: Standards, Quality Control, and Measurement Sciences in 3D Printing and Additive Manufacturing (2017).
3. C. W. J. Lim, K. Q. Le, Q. Y. Lu, and C. H. Wong: An overview of 3-D printing in manufacturing, aerospace, and automotive industries. *IEEE Potentials* **35**, 18–22 (2016).
4. C. Yan, L. Hao, A. Hussein, P. Young, and D. Raymont: Advanced lightweight 316L stainless steel cellular lattice structures fabricated via selective laser melting. *Mater. Des.* **55**, 533–541 (2014).
5. J. Zhou, P. Shrotriya, and W. Soboyejo: On the deformation of aluminum lattice block structures: from struts to structures. *Mech. Mater.* **36**, 723–737 (2004).
6. S. Fatemi, J. Ashany, A. Aghchai, and A. Abolghasemi: Experimental investigation of process parameters on layer thickness and density in direct metal laser sintering: a response surface methodology approach. *Virtual. Phys. Prototyp.* **12**, 133–140 (2017).
7. D. Do and P. Li: The effect of laser energy input on the microstructure, physical and mechanical properties of Ti-6Al-4 V alloys by selective laser melting. *Virtual. Phys. Prototyp.* **11**, 41–47 (2016).
8. B. AlMangour, D. Grzesiak, T. Borkar, and J. Yang: Densification behavior, microstructural evolution, and mechanical properties of TiC/316L stainless steel nanocomposites fabricated by selective laser melting. *Mater. Des.* **138**, 119–128 (2018).
9. M. X. Gan and C. H. Wong: Properties of selective laser melted spodumene glass-ceramic. *J. Eur. Ceram. Soc.* **37**, 4147–4154 (2017).
10. I. Yadroitsev, P. Bertrand, and I. Smurov: Parametric analysis of the selective laser melting process. *Appl. Surf. Sci.* **253**, 8064–8069 (2007).
11. S. Khairallah and A. Anderson: Mesoscopic simulation model of selective laser melting of stainless steel powder. *J. Mater. Process. Technol.* **214**, 2627–2636 (2014).
12. J. Kruth, L. Froyen, J. Van Vaerenbergh, P. Mercelis, M. Rombouts, and B. Lauwers: Selective laser melting of iron-based powder. *J. Mater. Process. Technol.* **149**, 616–622 (2004).
13. A. Matsunawa, J. Kim, N. Seto, M. Mizutani, and S. Katayama: Dynamics of keyhole and molten pool in laser welding. *J. Laser. Appl.* **10**, 247–254 (1998).
14. K. Kempen, L. Thijs, J. Van Humbeeck, and J. Kruth: Mechanical properties of AlSi10Mg produced by selective laser melting. *Phys. Procedia.* **39**, 439–446 (2012).
15. B. AlMangour, D. Grzesiak, J. Cheng, and Y. Ertas: Thermal behavior of the molten pool, microstructural evolution, and tribological performance during selective laser melting of TiC/316L stainless steel nanocomposites: Experimental and simulation methods. *J. Mater. Process. Technol.* **257**, 288–301 (2018).
16. T. Niendorf, S. Leuders, A. Riemer, H. Richard, T. Tröster, and D. Schwarze: Highly anisotropic steel processed by selective laser melting. *Metall. Mater. Trans. B* **44**, 794–796 (2013).
17. CFDEM®: LIGGGHTS Open Source Discrete Element Method Particle Simulation Code | CFDEM®project. [Online]. Available: https://www.cfdem.com/liggghts-open-source-discrete-element-method-particle-simulation-code.
18. OpenFOAM®: The open source CFD toolbox. OpenCFD Ltd, [Online]. Available: https://www.openfoam.com/.
19. C. Qiu, C. Panwisawas, M. Ward, H. Basoalto, J. Brooks, and M. Attallah: On the role of melt flow into the surface structure and porosity development during selective laser melting. *Acta Mater.* **96**, 72–79 (2015).
20. F. Rösler and D. Brüggemann: Shell-and-tube type latent heat thermal energy storage: numerical analysis and comparison with experiments. *Heat Mass Transf.* **47**, 1027–1033 (2011).
21. C. Panwisawas, C. Qiu, M. Anderson, Y. Sovani, R. Turner, M. Attallah, J. Brooks, and H. Basoalto: Mesoscale modelling of selective laser melting: thermal fluid dynamics and microstructural evolution. *Comput. Mater. Sci.* **126**, 479–490 (2017).
22. Z. Saldi: *Marangoni Driven free Surface Flows in Liquid Weld Pools*. (Delft University of Technology, The Netherlands, 2012).
23. J. Brackbill, D. Kothe, and C. Zemach: A continuum method for modeling surface tension. *J. Comput. Phys.* **100**, 335–354 (1992).
24. T. DebRoy and S. A. David: Physical processes in fusion welding. *Rev. Mod. Phys.* **67**, 85–112 (1995).
25. J. Cho, D. Farson, J. Milewski, and K. Hollis: Weld pool flows during initial stages of keyhole formation in laser welding. *J. Phys. D: Appl. Phys.* **42**, 175502 (2009).
26. C. Y. Yap, C. K. Chua, and Z. L. Dong: An effective analytical model of selective laser melting. *Virtual. Phys. Prototyp.* **11**, 21–26 (2016).
27. U. Scipioni Bertoli, A. Wolfer, M. Matthews, J. Delplanque, and J. Schoenung: On the limitations of volumetric energy density as a design parameter for selective laser melting. *Mater. Des.* **113**, 331–340 (2017).
28. M. Rombouts, J. Kruth, L. Froyen, and P. Mercelis: Fundamentals of Selective Laser Melting of alloyed steel powders. *CIRP Ann.* **55**, 187–192 (2006).
29. I. Yadroitsev, I. Yadroitsava, P. Bertrand, and I. Smurov: Factor analysis of selective laser melting process parameters and geometrical characteristics of synthesized single tracks. *Rapid. Prototyp. J.* **18**, 201–208 (2012).

https://doi.org/10.1557/mrc.2018.180 Published online by Cambridge University Press